A Hybrid Two-Phase Mixture Model of Detonation Diffraction with Compliant Confinement

D. W. Schwendeman [a], A. K. Kapila [a 1] and W. D. Henshaw [b]

[a] *Department of Mathematical Sciences, Rensselaer Polytechnic Institute, Troy, New York, 12180*

[b] *Center for Applied Scientic Computing, Lawrence Livermore National Laboratory, Livermore, California, 94550*

Abstract

A multi-material two-phase hybrid model of heterogeneous explosives, with a reaction rate that is proportional to the gas-phase pressure excess above an ignition threshold, is examined computationally. The explosive is confined within a compliant inert, and the focus is on the behavior of an established detonation as it rounds a 90° corner and undergoes diffraction. The numerical approach, a variant of Godunov's method, is designed to capture interfaces between materials that can undergo phase change, and extends previous work of the authors on rigidly-confined two-phase detonations. The dependence of the post-diffraction conduct on the strength of the confinement is explored by holding the reaction-rate prefactor and the ignition threshold fixed, and considering confiners of two different strengths. The aim is to determine whether a detonation that turns the corner successfully when rigidly confined can experience failure when the confinement is compliant.

Key words: Detonation; diffraction; dead zone; compliant confinement; multi-material two-phase model; interface capturing

1 Introduction

A high-energy granular explosive is a complex material containing polycrystalline grains of the energetic component, held together by a polymer and

1 . Corresponding author: A.K. Kapila, email: kapila@rpi.edu

possibly containing additives, impurities, voids, gas-filed pores, and the like. When a detonation is initiated by a stimulus such as a shock, the strongly heterogeneous material responds nonuniformly. Mechanical processes such as friction and pore collapse generate hot spots where chemical reaction originates preferentially before spreading to the bulk. Despite this heterogeneity at the grain scale, detonation fronts are remarkably smooth and reproducible when observed at a scale representative of the device, and are thus indicative of an intrinsic homogenization underlying the macro-scale response. Such complaisant behavior on the part of the explosive, coupled with the impracticability of routine computations that resolve the microstructure, has led to the development of continuum engineering models at the macro scale. These models treat the explosive either as a single-phase or a two-phase homogeneous mixture of reactant and product. Grain-scale processes are introduced as constitutive input, phenomenological rather than founded on a rational, ab-initio derivation that bridges the scales, and crucially dependent upon calibration with experiments.

The single-phase approach assumes that the two constituents, the reactant and the product, are in mechanical and thermal equilibrium and subject to a single reaction at a rate that attempts to incorporate microstructural effects. A well-studied example of this approach is the ignition-and-growth model originally proposed by Lee and Tarver [1] and later refined by Tarver and colleagues [2,3,4,5]. The two-phase approach recognizes explicitly the porous nature of the explosive, treating it as a mixture of two distinct but coexisting phases and allowing mutual exchange of mass, momentum and energy across the interfacial boundaries. Constitutive expressions for the interfacial exchange supplement the balance laws; they incorporate the micromechanical submodels and their formulation is constrained by thermodynamic principles. A prominent example of this approach is the two-phase model considered by Baer and Nunziato [6].

Given the somewhat ad hoc nature of these models, it is important to assess how well they perform in capturing and predicting observed phenomena in complicated geometries. When suitably calibrated, both types of models have well-replicated various aspects of planar, one-dimensional experiments; see, for example, Tarver and colleagues cited above for the ignition-and-growth model, and Baer and collaborators [6,7,8] for the two-phase model. Nonplanar geometries, however, have been a greater challenge. Consider, in particular, the appearance of dead zones in corner-turning. Experiments have shown that when a well-established detonation diffracts around a sharp corner, it leaves behind a sustained pocket of unreacted material, or a dead zone, in the vicinity of the corner [9,10,11]. In earlier studies we have demonstrated that the standard ignition-and-growth model does not admit dead zones for either rigid [12] or compliant [13] confinement. In a later study [14] we considered a modification of the ignition-and-growth model to account for the effect of desensitization by

weak shocks, and this enhanced model was shown to be capable of admitting dead zones. An alternate approach to desensitization was outlined in [15].

In recent work we have focused on the two-phase model and proposed a new numerical approach for it [16], which is a variant of the Godunov method and includes a rational treatment of the non-conservative nozzling terms of the model. We have employed it to examine in detail the initiation and propagation of a detonation following a weak planar impact in a one-dimensional configuration [17] as well as its possible failure as it negotiates sharp corners and undergoes diffraction [18]. These investigations assume a pressure-dependent reaction rate. We find, in particular, that the pressure threshold for ignition and the reaction-rate prefactor can indeed act in concert to produce dead zones by themselves, without the introduction of additional mechanisms. The diffraction study in [18] was restricted, however, to the explosive being confined within rigid walls. In this paper we relax this restrictive assumption and re-examine the post-diffraction behavior of an established detonation when the confining walls are compliant. Specifically, we explore whether a detonation that negotiates a sudden expansion successfully when confined rigidly can fail to do so when confined compliantly.

The explosive geometry is taken to be a slab with a sudden expansion, i.e., a narrow *donor* charge attached to a wider *acceptor* charge. The entire slab is surrounded by an inert, deformable medium whose lateral dimensions are large enough so that its outer boundary does not influence the computation over the time of interest. This configuration, motivated by the experiments of Ferm et al [9], is similar to that employed in [18]. The compliant confinement is chosen to be strong enough so that a steady, curved detonation is established in the donor charge by means of a high-pressure booster. As the detonation crosses into the acceptor charge, experiments show that upon diffraction the reaction zone peels away from the leading shock as the detonation goes around the corner, leading to the appearance of a dead zone in the vicinity of the corner. We demonstrate that while a rigid confinement tends to suppress dead zones, a compliant confinement can indeed promote their development.

The presence of the compliant confiner requires that the aforementioned numerical procedure designed for the two-phase reactive model be suitably extended to accommodate what is now a more complex system. The extension must ensure, in particular, that the interface separating the explosive and the confiner is computed accurately and robustly. This is done by treating the explosive-confiner system as a two-phase, two-material, *hybrid* mixture, so that the same set of equations apply everywhere in the domain. The two materials are the explosive and the confiner, and the term hybrid signifies that the explosive component is itself a two-phase mixture composed of the energetic solid and the product gas. The composition of the system is specified by a pair of material variables that advect with the solid-phase velocity. (A

more general situation involving multiple materials that would arise, for example, when there are inert inclusions embedded within the explosive, can be treated in a similar fashion by introducing additional compositional variables.) The interface between the explosive and the confiner is captured rather than tracked, by allowing it to have a finite thickness extending to a few computational cells in which both constituents coexist simultaneously. In the bulk of the computational domain outside the thin interfacial zones, a single material is effectively the lone component. Given the equations of state of the individual components, construction of the equation of state of the mixture, in general, requires some closure conditions, i.e., assumptions about mutual interaction between the constituents such as exchange of momentum and energy. Since the mixture is introduced purely as a numerical construct designed to facilitate the treatment of the interface, we are afforded a greater latitude in the selection of closure conditions. In particular, we base our choice on considerations of computational convenience and robustness rather than on any preconceived physics of the interface. Our mathematical formulation further assumes that certain constitutive parameters advect with the mixture, which follows similar formulations used by others, see for example the work by Abgrall [19] and Saurel and Abgrall [20]. The numerical approach used to compute solutions of the governing equations is a high-resolution Godunov scheme which is an amalgamation of that described in [18] for the equations modeling two-phase reactive flow and in [21] for the equations modeling the collapse of a cavity. The approach employs the exact solution of a Riemann problem to compute numerical fluxes and to advance the constitutive parameters which determine the state of the mixture and are governed by non-conservative advection equations.

The subsequent sections of the paper begin with a discussion of the governing equations in Section 2. Section 3 describes the configuration, lists the parameter set and identifies the reference scales. The numerical method used to compute solutions of the equations is described in Section 4, and the results are given in Section 5. Conclusions from our numerical study are drawn in Section 6.

2 Governing equations

The explosive/confiner system is treated as a multi-material mixture consisting of the explosive and the inert confiner, of which the explosive component is itself a two-phase mixture composed of the unreacted energetic material and the detonation product. The detonation product is a gas, and even though we shall continue to refer to the unreacted material as a solid, it is customary to model it as a fluid because of the high pressures involved. Each phase of the explosive obeys separate balance laws of mass, momentum and energy,

plus an equation that allows compaction of the solid phase driven by the pressure difference between phases. Terms representing interfacial exchange of mass, momentum and energy appear, corresponding to the non-equilibrium processes of reaction, drag and heat transfer.

2.1 Standard two-phase model

We begin by presenting the equations for the explosive component first, and then consider an extension of the model to include the confiner. The equations are essentially those first proposed by Baer and Nunziato [6], with some modifications suggested by Bdzil et al [22], and are the same as were used in our earlier study [18]. Although the computational configuration is two-dimensional, we write down the equations in one space dimension for ease of presentation. Thus,

$$\frac{\partial}{\partial t}\mathbf{u} + \frac{\partial}{\partial x}\mathbf{f}(\mathbf{u}) = \mathbf{h}(\mathbf{u})\frac{\partial \bar{\alpha}}{\partial x} + \mathbf{k}(\mathbf{u}), \tag{1}$$

with

$$\mathbf{u} = \begin{bmatrix} \bar{\alpha} \\ \bar{\alpha}\bar{\rho} \\ \bar{\alpha}\bar{\rho}\bar{v} \\ \bar{\alpha}\bar{\rho}\bar{E} \\ \alpha\rho \\ \alpha\rho v \\ \alpha\rho E \end{bmatrix}, \quad \mathbf{f}(\mathbf{u}) = \begin{bmatrix} 0 \\ \bar{\alpha}\bar{\rho}\bar{v} \\ \bar{\alpha}(\bar{\rho}\bar{v}^2 + \bar{p}) \\ \bar{\alpha}\bar{v}(\bar{\rho}\bar{E} + \bar{p}) \\ \alpha\rho v \\ \alpha(\rho v^2 + p) \\ \alpha v(\rho E + p) \end{bmatrix}, \quad \mathbf{h}(\mathbf{u}) = \begin{bmatrix} -\bar{v} \\ 0 \\ +p \\ +\bar{v}p \\ 0 \\ -p \\ -\bar{v}p \end{bmatrix}, \quad \mathbf{k}(\mathbf{u}) = \begin{bmatrix} \mathcal{F} + \mathcal{C}/\bar{\rho} \\ +\mathcal{C} \\ +\mathcal{M} \\ +\mathcal{E} - p\mathcal{F} \\ -\mathcal{C} \\ -\mathcal{M} \\ -\mathcal{E} + p\mathcal{F} \end{bmatrix}. \tag{2}$$

Here, α is the volume fraction, ρ the density, v the velocity, p the pressure and E the total energy. The bar superscript denotes solid-phase variables while gas-phase variables have no superscript. The total energy of each phase is given by

$$E = e + \frac{v^2}{2}, \qquad \bar{E} = \bar{e} + \frac{\bar{v}^2}{2},$$

where e is the specific internal energy of the gas and

$$\bar{e}_s = \bar{e} + \bar{B}(\bar{\alpha}) + \bar{q}$$

is the specific internal energy of the solid. The internal energy of the solid is the sum of the internal energy of the pure solid $\bar{e}$, the compaction potential energy $\bar{B}(\bar{\alpha})$ and the heat release $\bar{q}$. The compaction potential accounts for

the configuration-dependent energy of the solid. We take

$$\bar{B}(\bar{\alpha}) = \frac{(p_0 - \bar{p}_0)(2-\bar{\alpha}_0)^2}{\bar{\alpha}_0\bar{\rho}_0 \ln(1-\bar{\alpha}_0)} \ln\left[\left(\frac{2-\bar{\alpha}_0}{2-\bar{\alpha}}\right)\frac{(1-\bar{\alpha})^{(1-\bar{\alpha})/(2-\bar{\alpha})}}{(1-\bar{\alpha}_0)^{(1-\bar{\alpha}_0)/(2-\bar{\alpha}_0)}}\right],$$

where the zero subscript denotes quantities given by a reference ambient state. In addition, we employ a virial equation of state for the gas phase and a stiffened equation of state for the solid phase so that

$$e(\rho, p) = \frac{p}{(\gamma-1)\rho(1+b\rho)}, \qquad \bar{e}(\bar{\rho}, \bar{p}) = \frac{\bar{p} + \bar{\gamma}\bar{\pi}}{(\bar{\gamma}-1)\bar{\rho}}, \tag{3}$$

where γ and $\bar{\gamma}$ are ratios of specific heats, b is a virial gas coefficient, and $\bar{\pi}$ is a solid stiffening pressure. Finally, the volume fractions satisfy the saturation constraint,

$$\alpha + \bar{\alpha} = 1.$$

Source terms representing interactions between the phases appear on the right-hand side of the equations in (2). The terms proportional to $\bar{\alpha}_x$ are the so-called nozzling terms. They arise naturally in the model and describe momentum and energy exchange between the phases as the result of an effective change in the cross-sectional area of a virtual stream tube in the gas phase. The undifferentiated sources terms on the right-side of (2) represent compaction, $\mathcal{F}$, compaction work, $p\mathcal{F}$, and an exchange of mass, momentum and energy between phases given by $\mathcal{C}$, $\mathcal{M}$ and $\mathcal{E}$, respectively. A number of choices for $\mathcal{C}$ can be made depending on the assumed kinetics of the chemical reactions. Following [18] we let

$$\mathcal{C} = \begin{cases} 0 & \text{if } p < p_{\text{ign}}, \\ -\sigma\bar{\alpha}\bar{\rho}(p - p_{\text{ign}}) & \text{if } p \geq p_{\text{ign}}, \end{cases} \tag{4}$$

where $\sigma > 0$ is a rate constant and p_{ign} is an ignition pressure. The other quantities in the source terms are assumed to have the form

$$\mathcal{F} = \alpha\bar{\alpha}(\bar{p} - p - \bar{\beta})/\mu_c, \tag{5}$$

$$\mathcal{M} = \bar{v}\mathcal{C} + \left(\delta + \tfrac{1}{2}\mathcal{C}\right)(v - \bar{v}), \tag{6}$$

$$\mathcal{E} = (\bar{E} + \beta/\bar{\rho})\mathcal{C} + \left(\delta + \tfrac{1}{2}\mathcal{C}\right)\left((v-\bar{v})\bar{v}\right) + H(T - \bar{T}), \tag{7}$$

where μ_c is the compaction viscosity, δ is the drag coefficient, $\beta = \bar{\alpha}\bar{\rho}\bar{B}'(\bar{\alpha})$ is the configuration pressure, H is the heat-transfer coefficient, and T and $\bar{T}$ are the temperatures of the gas and solid, respectively. These temperatures are given by

$$C_v T = \frac{p}{(\gamma-1)\rho(1+b\rho)}, \qquad \bar{C}_v\bar{T} = \frac{\bar{p} + \bar{\gamma}\bar{\pi}}{(\bar{\gamma}-1)\bar{\rho}},$$

where C_v and $\bar{C}_v$ are specific heats at constant volume. More details on the interaction terms can be found in [18].

2.2 Hybrid two-phase mixture model

With the description of the explosive component in place, the equation set can now be extended to apply to the hybrid mixture. The balance equations remain the same as in (1) above, but now the solid phase is a multi-component mixture. The major components are the explosive and the inert confiner. For the problem at hand there is also a third component, a secondary explosive, capable of being readily set off so that it acts as a booster charge to initiate the primary explosive. The distribution of the three components in the mixture is described by the identifier function $\bar{\mu}_0$, defined initially over the entire computational domain as

$$\bar{\mu}_0 = \begin{cases} 0 & \text{in the inert confiner,} \\ 1 & \text{in the primary explosive, and} \\ 2 & \text{in the secondary explosive booster.} \end{cases}$$

Across a sharp interface $\bar{\mu}_0$ would jump, but here the interfaces though thin are smeared, and across each interface $\bar{\mu}_0$ is prescribed to vary smoothly but rapidly between the values on either side of the interface. It is also assumed to advect with the solid-phase velocity, i.e.,

$$\frac{\partial \bar{\mu}_0}{\partial t} + \bar{v}\frac{\partial \bar{\mu}_0}{\partial x} = 0. \tag{8}$$

Like the primary explosive, the other two solid components, the inert confiner and the secondary explosive, are also modeled as compressible fluids, each with a stiffened-gas equation of state of the form (3b). We introduce constitutive variables $\bar{\mu}_1$ and $\bar{\mu}_2$, defined by

$$\bar{\mu}_1 = \frac{1}{\bar{\gamma} - 1}, \quad \bar{\mu}_2 = \frac{\bar{\gamma}\bar{\pi}}{\bar{\gamma} - 1},$$

which are also assumed to advect with the solid phase, i.e.,

$$\frac{\partial \bar{\mu}_j}{\partial t} + \bar{v}\frac{\partial \bar{\mu}_j}{\partial x} = 0, \qquad j = 1,\ 2. \tag{9}$$

The mixture internal energy for the solid phase is determined by

$$\bar{e} = \frac{1}{\bar{\rho}}(\bar{\mu}_1 \bar{p} + \bar{\mu}_2) + \bar{q},$$

where $\bar{q}$ is specified by μ_0. Initially, the triple $(\bar{\gamma}, \bar{\pi}, \bar{q})$ is defined separately for the three components as

$$(\bar{\gamma}, \bar{\pi}, \bar{q}) = \begin{cases} (\bar{\gamma}_e, \bar{\pi}_e, Q_e) & \text{in the primary explosive,} \\ (\bar{\gamma}_b, \bar{\pi}_b, Q_b) & \text{in the secondary explosive booster, and} \\ (\bar{\gamma}_i, \bar{\pi}_i, 0) & \text{in the inert confiner.} \end{cases}$$

3 Configuration, parameter set and reference scales

The configuration under study is illustrated in Figure 1. Only the lower half below the plane of symmetry is shown. The explosive sample is L-shaped, with the primary explosive forming the donor and the acceptor segments and the secondary explosive comprising the booster segment. The inert confiner encloses the sample. It is noted that in the initial state shown in Figure 1

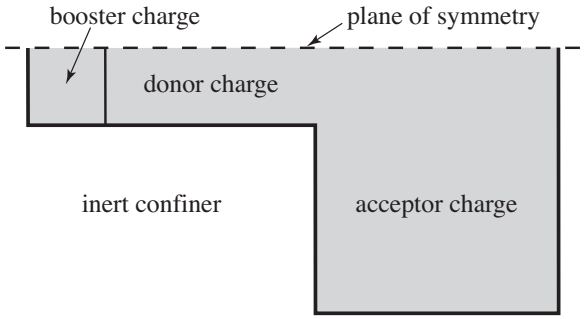

Figure 1. Initial configuration for corner turning. A detonation in the donor segment, initiated by the booster, will propagate to the right and diffract into the acceptor segment.

the interfaces are sharp and the components are separated, so that there is no region where two or more solids coexist to form a mixture. In the exact solution such a state would persist as the flow evolves, but in the numerical approximation a mixture exists right at the outset as the interfaces are smeared initially over two or three grid cells. The smeared regions are thin and purely numerical, and we assign no particular physical significance to the state of the flow within such regions.

For the computations a representative primary explosive is considered with the following ambient state:

Gas phase:	$\alpha_0 = .27,$	$\rho_0 = 1$ kg/m^3,	$p_0 = .25225$ MPa,	$T_0 = 300$ K,
Solid phase:	$\bar{\alpha}_0 = .73,$	$\bar{\rho}_0 = 1900$ kg/m^3,	$\bar{p}_0 = 7.6$ MPa,	$\bar{T}_0 = 300$ K.

The equation-of-state parameters for the explosive are chosen to be

$$\begin{aligned} &\text{Gas phase:} \quad \gamma = 1.35, \quad b = 0.001 \text{ m}^3/\text{kg}, \quad C_v = 2400 \text{ J}/(\text{kg K}), \\ &\text{Solid phase:} \quad \bar{\gamma} = 5, \quad \bar{\pi} = 3412.4 \text{ MPa}, \quad \bar{C}_v = 1500 \text{ J}/(\text{kg K}), \end{aligned}$$

and the heat release is

$$\bar{q} = Q_e = 6.65 \times 10^6 \text{ J/kg}.$$

Two possible types of inert confiner, weak and strong, will be considered. In either case it is assumed that the confiner is essentially all solid and in mechanical and thermal equilibrium with the explosive. The weak confiner is modeled by air-like properties, and the strong confiner is taken to have the same physical properties as the explosive (with reaction set to zero of course). In the confiner $\bar{\alpha}_0 \approx 1$ and the equation-of-state parameters are

$$(\bar{\gamma}, \bar{\pi}) = \begin{cases} (5, 3412.4 \text{ MPa}), & \text{strong confinement}, \\ (1.4, 0), & \text{weak confinement}. \end{cases} \tag{10}$$

The secondary explosive in the booster is also taken to be very nearly all solid, with the same equation of state as the primary explosive but with a higher heat of reaction, $Q_b = 2.5 Q_e$, and a very low ignition pressure, $p_{\text{ign}} = 0$.

The initial state and the exothermicity of the primary explosive allow its Chapman-Jouget state to be determined (see [17]). It is found that the CJ detonation velocity is

$$D_{\text{CJ}} = 7508.8 \text{ m/s},$$

and the corresponding density, velocity, pressure and temperature are

$$\begin{aligned} &\rho_{\text{CJ}} = 1906.2 \text{ kg/m}^3, \qquad v_{\text{CJ}} = 2044.3 \text{ m/s}, \\ &p_{\text{CJ}} = 21.300 \text{ GPa}, \qquad T_{\text{CJ}} = 4577.1 \text{ K}. \end{aligned}$$

The CJ state, along with the choices

$$t_{\text{ref}} = 1 \ \mu\text{s}, \qquad C_{v,\text{ref}} = 2400 \text{ J}/(\text{kg K}), \tag{11}$$

is chosen to provide the reference scales,

$$\begin{aligned} &v_{\text{ref}} = D_{\text{CJ}} = 7508.8 \text{ m/s}, && p_{\text{ref}} = p_{\text{CJ}} = 21.300 \text{ GPa}, \\ &x_{\text{ref}} = v_{\text{ref}} t_{\text{ref}} = 7.5088 \times 10^{-3} \text{ m}, && \rho_{\text{ref}} = p_{\text{ref}}/v_{\text{ref}}^2 = 377.78 \text{ kg/m}^3, \\ &T_{\text{ref}} = v_{\text{ref}}^2/C_{v,\text{ref}} = 23492 \text{ K}, && E_{\text{ref}} = v_{\text{ref}}^2 = 5.6381 \times 10^7 \text{ J/kg}. \end{aligned} \tag{12}$$

Param.	Value	Param.	Value
$\bar{\alpha}_0$	0.73	$\bar{\gamma}$	5
$\bar{\rho}_0$	5.0293	$\bar{\pi}$	0.16021
$\bar{p}_0$	3.5682e−4	$\bar{C}_v$	0.625
$\bar{T}_0$	1.2770e−2	$\bar{q}$	0.11795
ρ_0	2.6470e−3	γ	1.35
p_0	1.1843e−5	b	0.37778
T_0	1.2770e−2	C_v	1

Table 1
Dimensionless upstream state and equation of state parameters.

Dimensionless quantities may now be defined in the usual way by dividing each dimensional quantity by its corresponding reference scale given in (11) or (12). The result leaves the governing equations in (1) unchanged. The corresponding dimensionless initial state and the equation of state parameters for the entire configuration are listed in Table 1. In addition, we require dimensionless parameters for the compaction viscosity in (5), the drag coefficient in (6), and the heat transfer coefficient in (7). For the purposes of this paper, we choose nominal values from the range of values considered in [17]. These dimensionless values are

$$\mu_c = 0.05, \qquad \delta = 20.0, \qquad \mathcal{H} = 0.2\ .$$

The remaining parameters of the two-phase model, σ and p_{ign}, are needed for the reaction rate in (4), and these will be chosen later in Section 5 for the particular numerical experiments studied.

4 Numerical approach

The equations governing the hybrid two-phase mixture model in (1), (8) and (9) form a hyperbolic system of nonlinear partial differential equations. This system, extended to two dimensions, can be written in the general form

$$\frac{\partial}{\partial t}\mathbf{U} + \frac{\partial}{\partial x_i}\mathbf{F}_i(\mathbf{U}) = A_i(\mathbf{U})\frac{\partial}{\partial x_i}\mathbf{U} + \mathbf{K}(\mathbf{U}), \tag{13}$$

with Einstein summation convention used. Here, $\mathbf{U}$ denotes the state variables, $\mathbf{F}_i$ the conserved fluxes, $A_i\mathbf{U}_{x_i}$ the non-conservative nozzling and advection terms, and $\mathbf{K}$ the non-differentiated source terms. Our numerical approach for (13) is a high-resolution shock-capturing method. The basic approach is discussed in [18] for the standard two-phase model, and its extension to han-

dle the advection equations that describe the solid-phase mixture follows the approach discussed in [21]. The numerical approach employs adaptive mesh refinement (AMR) following the approach described in [23], and it uses an extension to parallel computing following the work in [24]. Since the essential components of the numerical method are discussed in detail elsewhere, we provide only a brief summary of the approach here.

A Cartesian grid with equal mesh spacings covers the domain of interest and forms the base grid for AMR. Refinement grids are built on top of the base grid in a hierarchical fashion according to an estimate of the error. The solution in the vicinity of shocks and contact discontinuities is represented on the finest grid level, and refinement grids are also generated near sharp layers of reaction and/or interphase relaxation, so that a well-resolved numerical solution on the grid is obtained economically. In addition, each grid in the AMR system may be partitioned and computed in parallel. The partitioning of the grids and their distribution among a set of processors is done using a load-balancing algorithm. The parallel, AMR approach provides good speed up of the calculations, so that well-resolved solutions are obtained for the results discussed below.

The numerical solution of the governing equations in (13) are advanced on the base grid and on each refinement grid using a second-order slope-limited extension of Godunov's method. Solutions of the associated Riemann problems for Godunov's method are used to evaluate the conservative fluxes and the non-conservative nozzling and advective terms. We use exact solutions of the Riemann problems for the numerical scheme as this was found to give more accurate results than the corresponding ones using approximate Riemann solvers, such as an HLLC solver. The non-differentiated source terms are integrated numerically using a second-order Runge-Kutta error-control scheme, and this is incorporated into the scheme using a second-order Strang time-splitting approach. The essential components of the overall scheme were shown to be second-order accurate for smooth flows in [18] and [21]. It was shown further that well-resolved and accurate results were obtained for solutions with shocks, detonations and contacts.

5 Numerical results

The primary goal of this study is to explore the influence of a compliant confiner on the post-diffraction behavior of the detonation. Accordingly, we have elected to consider confiners of two different strengths: a strong confiner whose physical properties are the same as those of the unreacted explosive and a weak confiner whose properties are those of ambient air. Each is assumed to have a stiffened-gas equation of state, and the relevant parameters are

specified in (10). The post-diffraction behavior is also crucially influenced by the reaction rate, i.e., by the choices of the prefactor σ and the gas-pressure threshold for ignition p_{ign} appearing in expression (4) for the reaction rate. In [18], four different cases corresponding to different values of the reaction-rate parameters, listed in Table 2, were considered for investigating the post-diffraction scenario under rigid confinement.

Case	σ	p_{ign}
I	10	0.45
II	10	0.48
III	25	0.48
IV	25	0.53

Table 2
Reaction pre-factor σ and ignition threshold p_{ign} for Cases I, II, III and IV in [18].

It was found that in all cases, diffraction past the corner created a region of extinguished reaction in the vicinity of the corner, owing to an expansion-caused drop in the gas-phase pressure below p_{ign} at that location. The loss of reactive support weakened the gas-phase shock even more than the diffraction-induced expansion alone. Away from the corner the drop in the gas-phase pressure was less severe and the reaction continued, albeit at a reduced rate. The reduction in rate caused the gas-phase shock to lose speed, but to a much lesser extent than in the region away from the corner. A gradient of shock speed, and an associated gradient of post-shock gas-phase pressure, setup along the gas-phase shock, drove the reaction-supported segment of this shock towards the wall, allowing it to overtake the unsupported segment of the shock there and thereby raising the local gas-phase pressure and reviving the reaction. The extent of revival depended upon a delicate balance between the reaction-rate prefactor σ and the ignition threshold p_{ign}. For cases I and III the revival was strong enough to overcome the temporary extinction and regenerate a detonation, while cases II and IV exhibited sustained regions of extinguished reaction.

In this paper we undertake an investigation of Case III as an example of a representative situation that did not exhibit a dead zone under rigid confinement, to determine whether this behavior changes when the confinement is compliant.

5.1 Rate stick

The corner-turning study assumes that a steady detonation has been established in the narrow donor section of the test configuration, otherwise known

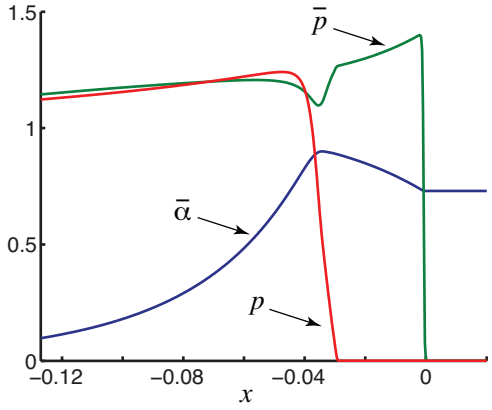

Figure 2. Steady, one-dimensional structure of the rigidly-confined detonation.

as a rate stick, upstream of the corner. A brief description of the structure of this detonation is given below for case III, $\sigma = 25$ and $p_{\text{ign}} = 0.48$. It was shown in [18] that for rigid confinement the steady, planar detonation for this case has a one-dimensional structure that is compaction-led. In other words, a lead shock in the solid is followed by a shock in the gas, and between the two shocks lies a compaction layer in which the solid volume fraction rises from the ambient value at the solid shock to a maximum at the gas shock, the peak value being below the full-compaction value of unity. The gas pressure rises to a level above p_{ign} at the gas shock, which then serves as the leading edge of a reaction zone that extends behind the gas shock and in which the solid volume fraction declines as the reactant is consumed. The structure is displayed in Figure 2 where profiles of solid volume fraction, solid pressure and gas pressure are plotted.

We now turn to the compliantly-confined rate stick. In it the detonation is initiated, computationally, by the attached booster charge supplying a high-pressure stimulus (1). The case of strong confinement is considered first, for which Figure 3 displays shaded contour plots of solid volume fraction and gas pressure at two different times. These plots show that the initially square booster region expands rapidly due to the high pressure generated within it, deflecting the explosive-confiner interface outwards and sending a detonation traveling in the explosive. As a result of the pressure release at the interface the detonation front is curved, and the detonation approaches a steady state as it propagates down the rate stick. The structure of the steady detonation along the plane of symmetry of the configuration is shown in Figure 4. We note that the structure is qualitatively similar to the rigidly-confined case shown in Figure 2, but the detonation speed is slower, the reaction zone wider and the peak pressures lower in both the solid and the gas. The expanded plots in Figure 5 show that along the curved detonation front the gas pressure drops from the plane of symmetry towards the explosive-confiner interface, thereby progressively weakening the reaction and broadening the reaction zone. Although

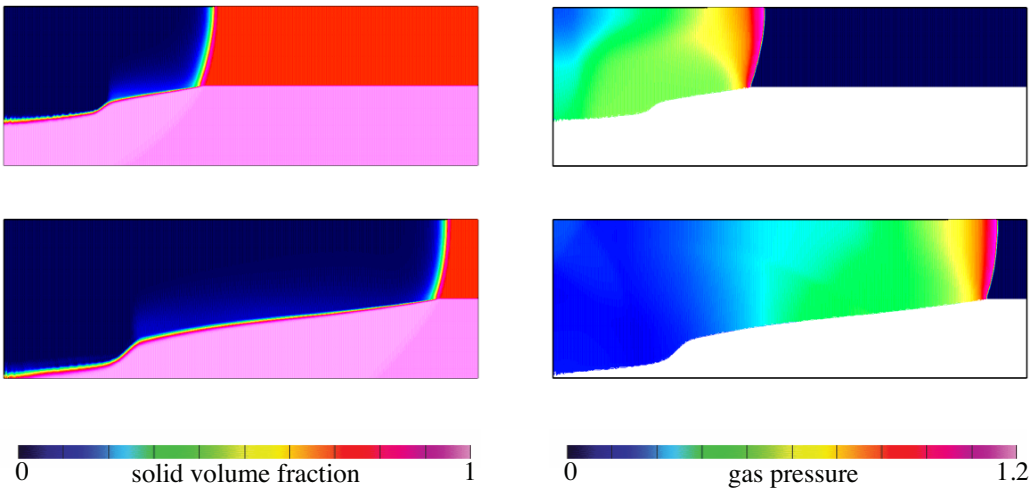

Figure 3. Strong confinement: shaded contour plots of solid volume fraction and gas pressure for $t = 1.5$ (top) and $t = 4.0$ (bottom).

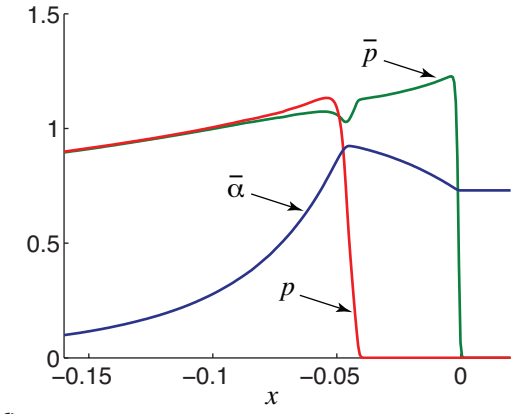

Figure 4. Structure of the strongly-confined detonation at the symmetry plane.

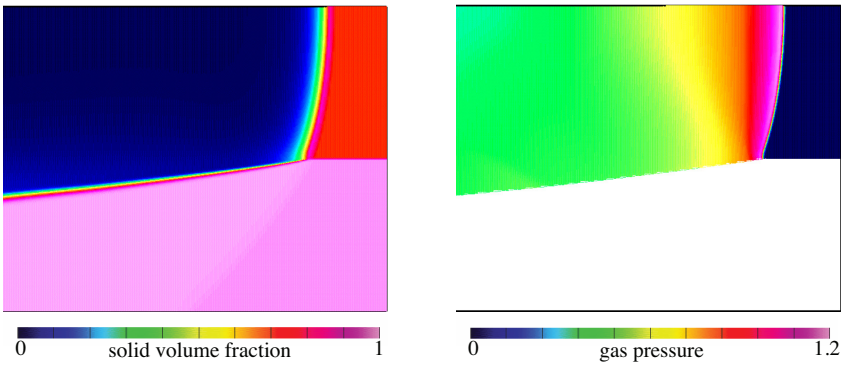

Figure 5. Expanded views of the wavefront of the strongly-confined detonation at $t = 4.0$: shaded contour plots of solid volume fraction (left) and gas pressure (right).

diminished, the gas pressure does not fall below p_{ign} and the reaction zone remains intact.

The weakly-confined detonation is considered next. Shaded contour plots of solid volume fraction and gas pressure at two different times are displayed in Figure 6 and the structure of the steady detonation along the plane of symmetry of the configuration is shown in Figure 7. Again, the structure is

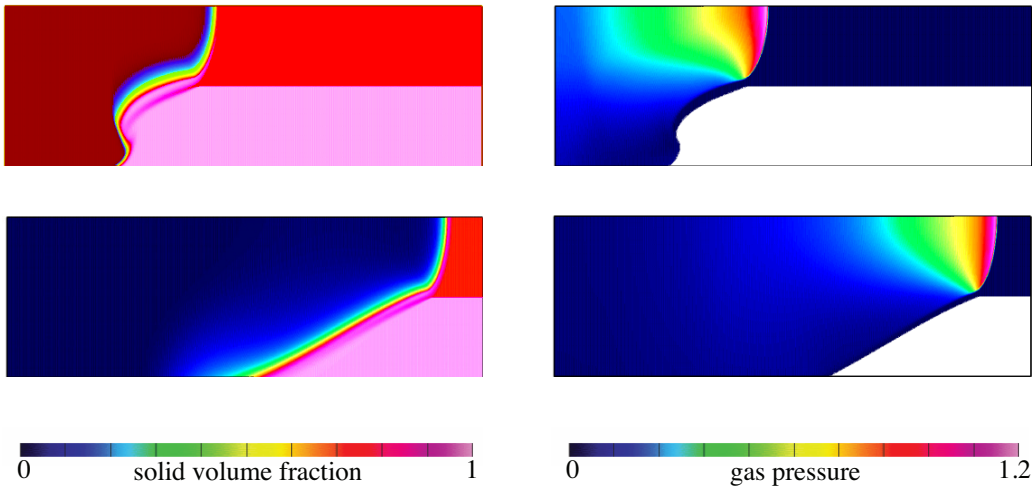

Figure 6. Weak confinement: shaded contour plots of solid volume fraction and gas pressure for $t = 1.5$ (top) and $t = 4.0$ (bottom).

qualitatively similar to those for rigid and strong confinements, but the reaction zone is wider still and the gas pressure and solid pressure peaks are yet smaller. Expanded views of the detonation front in Figure 8 show, as before,

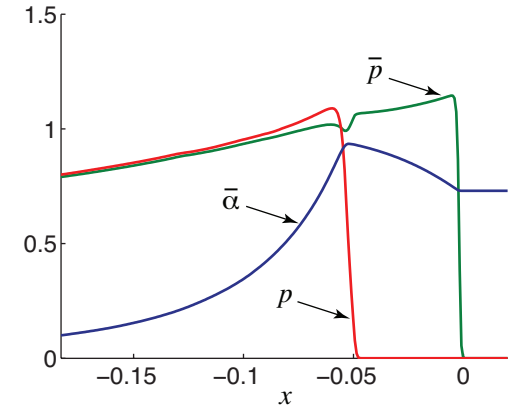

Figure 7. Structure of the weakly-confined detonation at the symmetry plane.

that as the detonation front curves away from the plane of symmetry the gas pressure along it drops and the reaction zone widens. For the weak confiner the gas pressure drops below p_{ign} before the confiner-explosive interface is reached, thereby extinguishing the reaction and leaving a thin layer of unreacted explosive trapped between the products of reaction and the confiner. In other words, a thin dead zone at the interface is a part of the steady detonation structure in the rate stick under weak confinement.

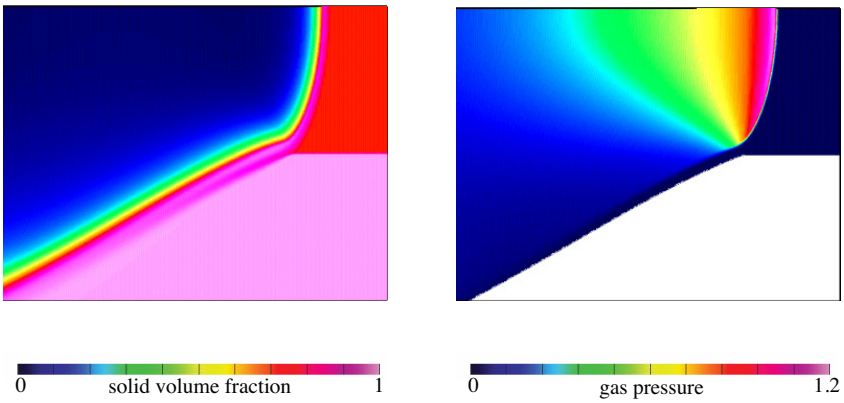

Figure 8. Expanded views of the wavefront of the weakly-confined detonation: shaded contour plots of solid volume fraction (left) and gas pressure (right).

5.2 Corner turning

We now present the results of diffraction as the detonation propagates from the donor into the acceptor section.

5.2.1 Strong confinement

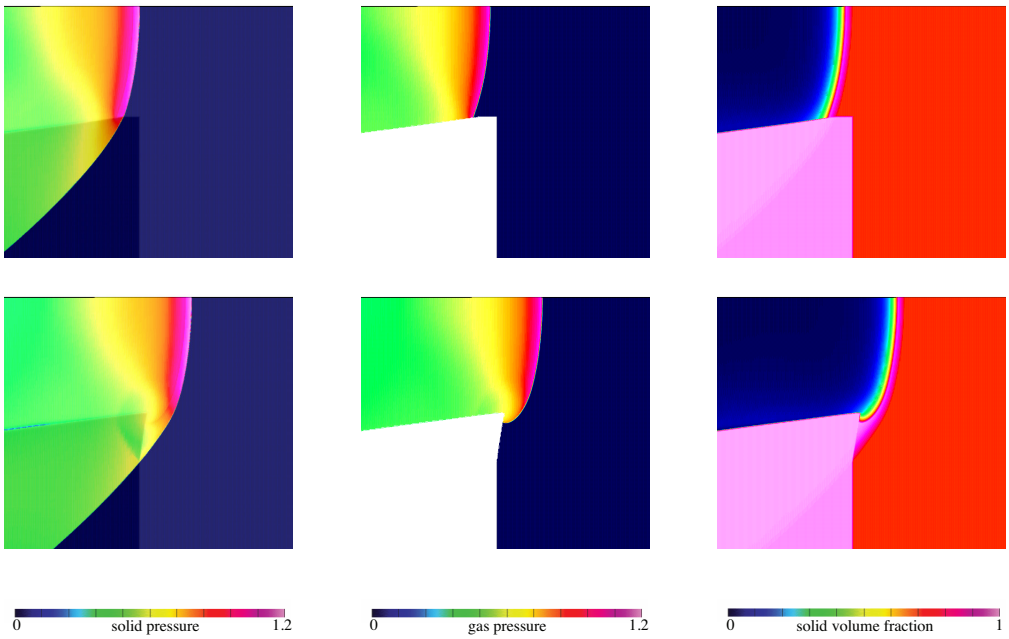

Figure 9. Strong confinement: solid pressure (left), gas pressure (middle) and solid volume fraction (right) at $t = 2.6$ (top frames) and $t = 3.0$ (bottom frames).

The numerical results for strong confinement are shown in Figures 9, 10 and 11. Figure 9 displays shaded contours of solid pressure, gas pressure and solid volume fraction at two times, just before and after the detonation front has

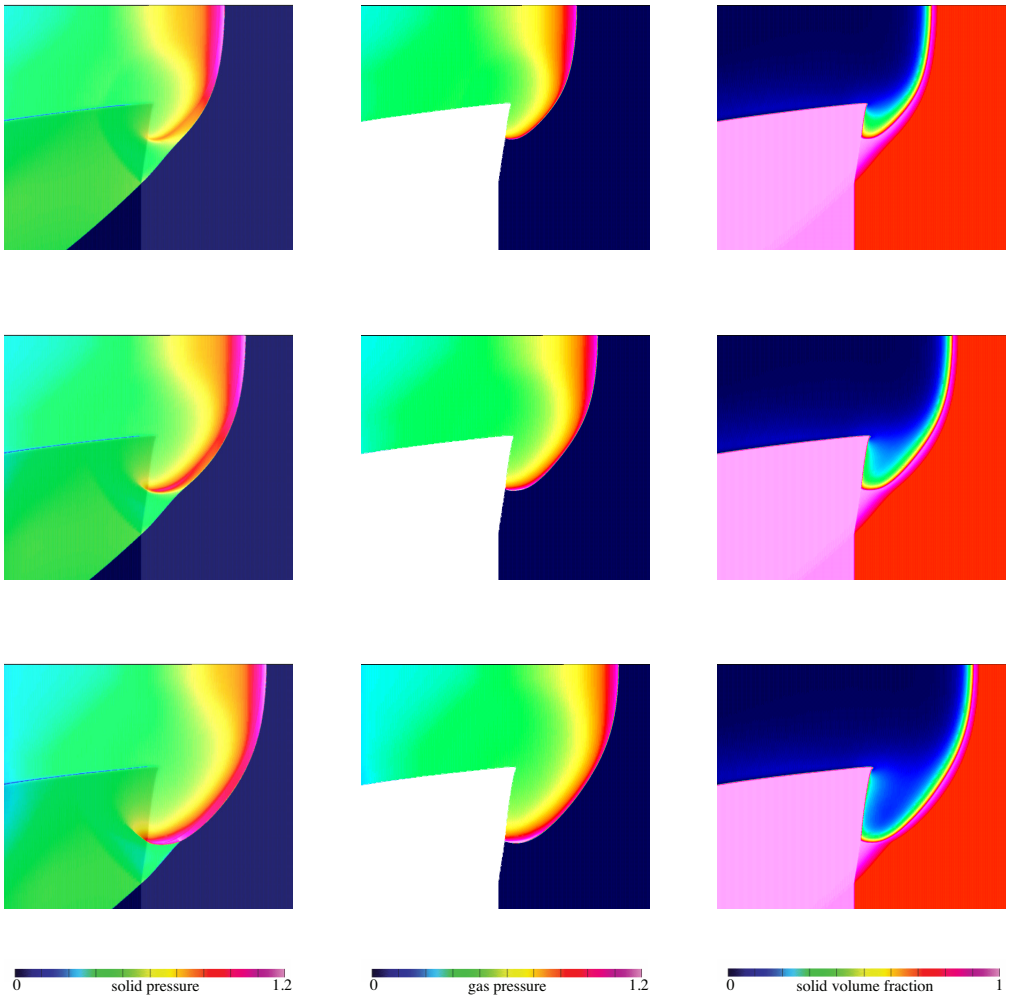

Figure 10. Strong confinement: solid pressure (left), gas pressure (middle) and solid volume fraction (right) at $t = 3.4$ (top frames), $t = 3.6$ (middle frames) and $t = 3.8$ (bottom frames).

passed the corner. At $t = 2.6$ the plots show a steady, curved front and a deflected interface separating the reaction products and the confiner, as was seen earlier for the rate stick. The solid shock leads the detonation, followed by the gas shock and then the reaction zone. Sandwiched between the two shocks is the compaction zone, nearly uniform in width across the detonation and most clearly seen in the solid volume fraction plot. An important feature visible in the solid pressure plot is the shock in the confiner which, being the result of pressure release across the hitherto horizontal interface but not directly supported by a reaction zone, is noticeably weaker than the solid shock that leads the detonation. At $t = 3.0$ the wave has gone past the corner. The portion of the front near the plane of symmetry is relatively unscathed by the passage into the acceptor region the but that in the vicinity of the corner is significantly affected. Two distinct segments now comprise the wavehead. Starting at the plane of symmetry and proceeding along the front, a bulk of

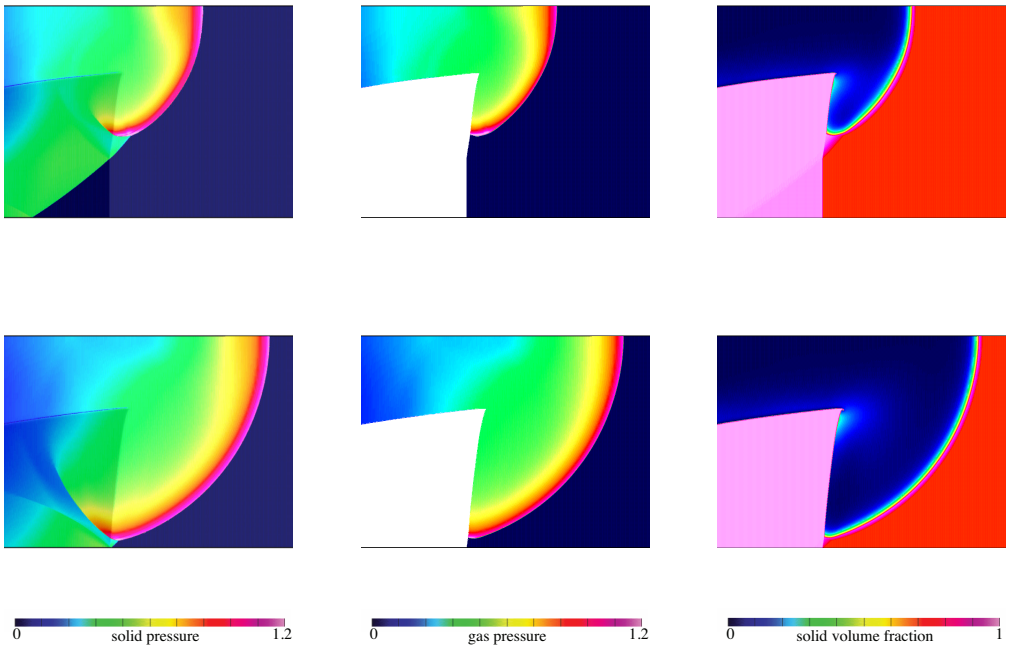

Figure 11. Strong confinement: solid pressure (left), gas pressure (middle) and solid volume fraction (right) at $t = 4.0$ (top frames) and $t = 5.0$ (bottom frames).

the wavehead forms a part of the detonation, i.e., the leading solid shock is supported by the reaction zone. However, the segment of the lead shock close to the corner and traveling down the left boundary of the acceptor charge is not a part of the detonation; it is simply a shock transmitted from the inert into the explosive across the aforementioned boundary. This segment is the weaker of the two, but is still capable of compacting the explosive. The bulk of the gas shock is also unaffected by passage across the corner, except for a small portion near the corner which has undergone diffraction and hence acquired additional curvature and suffered a loss in strength. Thus, corner turning leads to the following consequences: an increased separation between the solid and gas shocks near the corner and hence a wider compaction zone, as well as a reduced reaction rate behind the gas shock and hence a wider reaction zone. These features are again best viewed in the solid volume fraction plot.

The frames in Figure 10 display the behavior at three later times. One notes that at $t = 3.4$ the gas pressure around the corner has fallen just below the ignition threshold, leading to extinction of the reaction there. This extinction is confined to a narrow region and is quite local. Otherwise, on a broad segment of the inert-explosive interface at the left boundary of the acceptor charge for example, the gas pressure is high enough so that the reaction, although weak, is not shut off. In fact, the gas pressure at the gas shock and hence the reaction rate at that location are showing hints of strengthening. Further evidence of the revival can be seen in the plot of solid pressure, where an internal high

pressure ridge has begun to develop behind the wavehead. This revival is seen to gain vigor at $t = 3.6$ and at $t = 3.8$ one clearly sees a secondary detonation traveling down the explosive-inert interface. This trend continues in Figure 11, where plots for $t = 4.0$ and 5.0 are displayed. The secondary detonation has now overtaken the solid shock near the interface, and a nearly circular detonation is now advancing into the acceptor charge. Only a vestige of the partially-reacted explosive, or dead zone, can be seen in the vicinity of the corner in the solid volume fraction plot, where, as observed above, the reaction had suffered extinction. Otherwise the detonation has turned the corner successfully, as was the case for rigid confinement considered in [18].

5.2.2 Weak confinement

The numerical results for weak confinement are shown in Figures 12, 13 and 14. As above, shaded contours of solid pressure, gas pressure and solid volume fraction are displayed. Figure 12 shows plots for two times, just before and after the detonation front has passed the corner. At $t = 2.6$ the front is yet to reach the corner and the structure is that for the weakly-confined rate stick discussed above; the detonation has a curved structure similar to that for the strongly-confined case, with the exception that a thin dead zone of unreacted explosive is trapped between the detonation products and the confining inert. At $t = 3.2$ the detonation has passed into the acceptor charge, and diffraction-induced weakening has lowered the pressures at the front and expanded the size of the dead zone near the corner. Unlike the strongly-confined case, no precursor transmitted shock has passed from the inert into the acceptor charge. The plots of Figures 13 and 14 at later times show that the size of the dead zone expands, and that the detonation fails to turn the corner. This behavior is remarkably similar to the dead-zone observations seen in [9].

6 Conclusions

This paper presents a computational study of diffracting detonations in a compliantly-confined heterogeneous explosive, modeled as a two-phase reactive material consisting of the unreacted explosive (solid) and the product of reaction (gas). It complements our earlier study of detonation diffraction under rigid confinement [18]. The intent has been to determine whether a detonation that turns a right-angled corner successfully under rigid confinement can suffer failure and produce dead zones (pockets of extinguished reaction, observed experimentally in [9]) when confined by a compliant inert. Two different strengths of confinement are examined for a given explosive, whose reaction rate is taken to be proportional to gas-phase pressure excess above an ignition threshold.

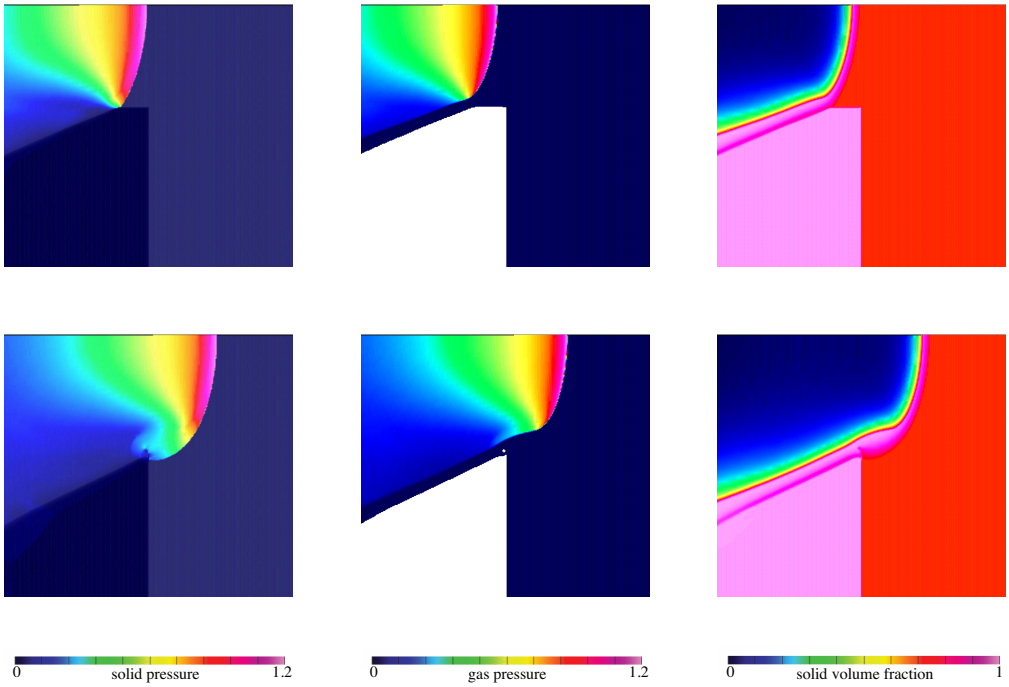

Figure 12. Weak confinement: solid pressure (left), gas pressure (middle) and solid volume fraction (right) at $t = 2.6$ (top frames) and $t = 3.2$ (bottom frames).

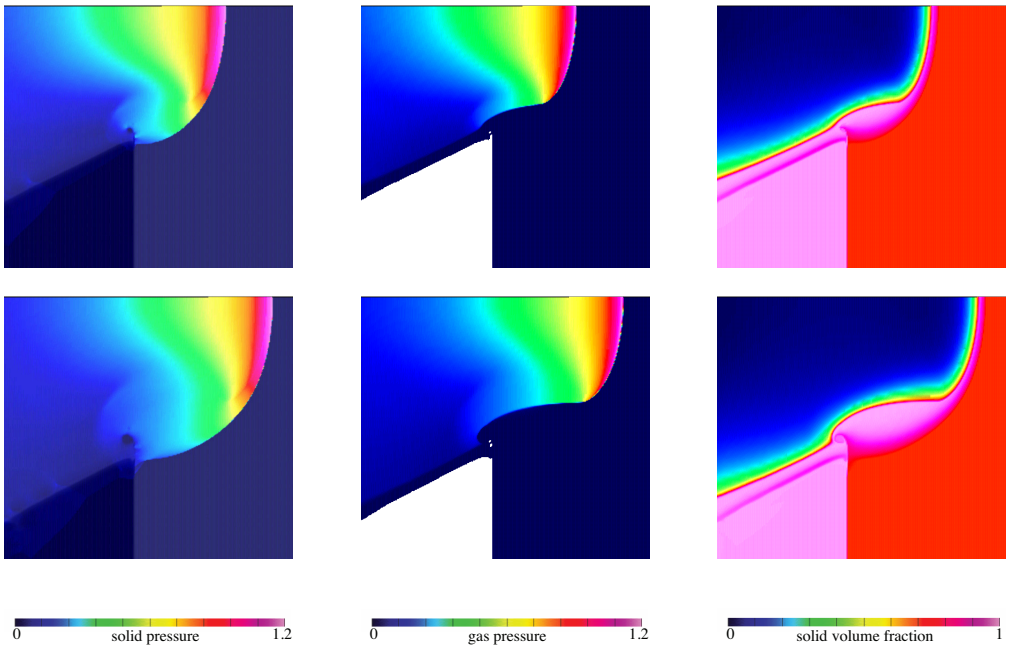

Figure 13. Weak confinement: solid pressure (left), gas pressure (middle) and solid volume fraction (right) at $t = 3.4$ (top frames) and $t = 3.8$ (bottom frames).

The explosive configuration consist of a narrow slab of reactive material, the donor section, suddenly expanding into a broader slab, the acceptor section.

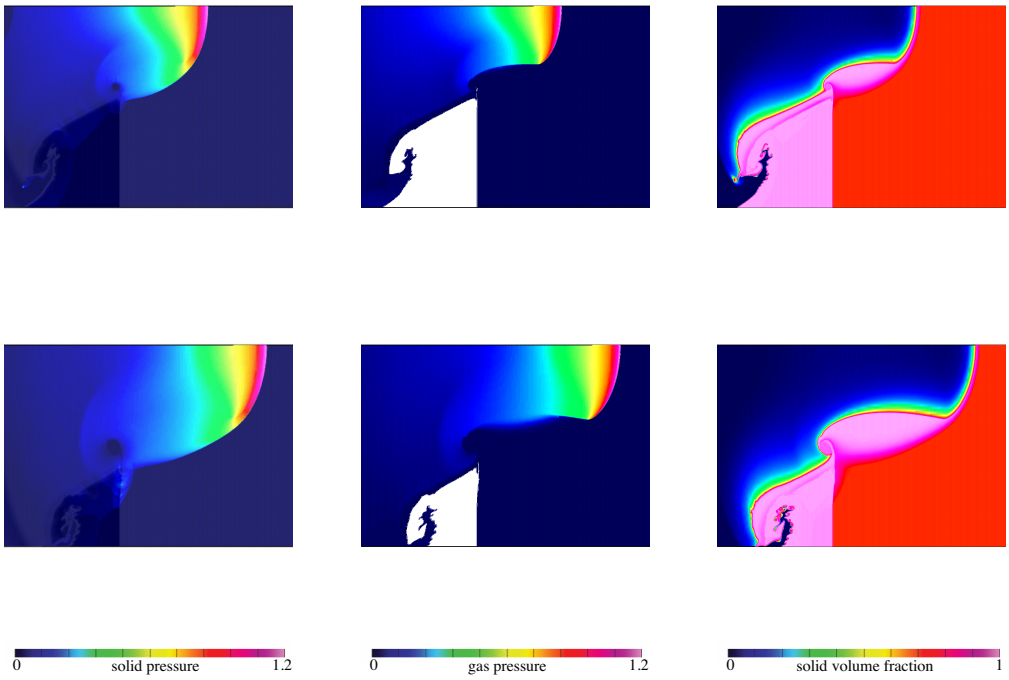

Figure 14. Weak confinement: solid pressure (left), gas pressure (middle) and solid volume fraction (right) at $t = 4.0$ (top frames) and $t = 5.0$ (bottom frames).

An inert, deformable confiner surrounds the explosive. Detonation in the donor section is initiated by means of an explosive booster. As the detonation travels down the donor section the confiner behind the detonation front is deflected by the high-pressure products of reaction, and the front itself acquires a curved shape. Pressure at the front is highest along the plane of symmetry and lowest at the interface with the inert. If the confiner is strong, then the lowest gas-phase pressure at the front remains above the ignition threshold, and the detonation proceeds without any sign of failure. If the confiner is sufficiently weak, then the gas pressure near the interface can fall below the ignition threshold and a thin layer of explosive near the interface remains unburned. In either case, passage of the detonation past the sharp corner lowers the gas-phase pressure further due to diffraction-induced expansion, and local regions of extinguished reaction can occur. Whether these regions persist, leading to sustained dead zones, or are consumed by a reaction-rate recovery, depends delicately upon the ignition threshold, the reaction-rate prefactor and the degree of compliance of the confiner. The detailed discussion of the previous section considers the possibililties and identifies the mechanisms that determine whether failure is transitory or sustained.

Acknowledgements

Research support for DWS and AKK was provided by the National Science Foundation (NSF) under grant DMS-1016188. Additional support for DWS was given by Lawrence Livermore National Laboratory (LLNL) under subcontract B548468. The work of WDH was performed under the auspices of the U.S. Department of Energy (DOE) by LLNL under Contract DE-AC52-07NA27344 and with the support of the ASCR Applied Math Program of the DOE Office of Science.

References

[1] E. L. Lee, C. M. Tarver, Phenomenological model of shock initiation in hetrogeneous explosives, Phys. Fluids 23 (12) (1980) 2362–2372.

[2] C. M. Tarver, J. O. Hallquist, L. M. Erickson, Modelling short-pulse duration shock initiation of solid explosives, in: The Eighth Symposium (International) on Detonation, 1985, pp. 951–960.

[3] C. M. Tarver, J. W. Kury, R. D. Breithaupt, Detonation waves in triaminonitrobenzene, J. Appl. Phys. 82 (1997) 3771–3782.

[4] J. W. Kury, R. D. Breithaupt, C. M. Tarver, Detonation waves in trinitrotoluene, Shock Waves 9 (1999) 227–237.

[5] C. M. Tarver, E. M. McGuire, Reactive flow modeling of the interaction of TATB detonation waves with inert materials, in: The Twelfth Symposium (International) on Detonation, 2002, pp. 641–649.

[6] M. R. Baer, J. W. Nunziato, A two-phase mixture theory for the deflagration-to-detonation transition (DDT) in reactive granular materials, Int. J. Multiphase Flow 12 (1986) 861–889.

[7] M. R. Baer, R. J. Gross, J. W. Nunziato, An experimental and theoretical study of deflagration-to-detonation transition (DDT) in the granular explosive CP, Combustion and Flame 65 (1986) 15–30.

[8] M. R. Baer, J. W. Nunziato, Compressive combustion of granular materials induced by low-velocity impact, in: The Ninth Symposium (International) on Detonation, 1989, pp. 293–305.

[9] E. Ferm, C. Morris, J. Quintana, P. Pazuchanic, H. Stacy, J. Zumbro, G. Hogan, N. King, Proton radiography examination of unburned regions in PBX 9502 corner turning experiments, Tech. Rep. LA-UR-01-3555, Los Alamos National Laboratory (2001).

[10] P. C. Souers, R. Garza, P. Vitello, Ignition and growth and JWL++ detonation models in course zones, Propellants, Explosives and Pyrotechnics 27 (2002) 62–71.

[11] C. M. Tarver, Ignition-and-growth modeling of LX-17 hockey puck experiments, Propellants, Explosives and Pyrotechnics 30 (2005) 109–117.

[12] A. K. Kapila, D. W. Schwendeman, J. B. Bdzil, W. D. Henshaw, A study of detonation diffraction in the ignition-and-growth model, Combust. Theory and Modeling 11 (2007) 781–822.

[13] J. B. Banks, D. W. Schwendeman, A. K. Kapila, W. D. Henshaw, A study of detonation propagation and diffraction with compliant confinement, Combust. Theory Modeling 12 (2008) 769–808.

[14] G. de Olivera, A. K. Kapila, D. W. Schwendeman, J. B. Bdzil, W. D. Henshaw, C. M. Tarver, Detonation diffraction, dead zones, and the ignition-and-growth model, in: The Thirteenth Symposium (International) on Detonation, 2006.

[15] B. L. Wescott, D. S. Stewart, W. C. Davis, Modeling diffraction and dead zones in PBX-9502, in: The Thirteenth Symposium (International) on Detonation, 2006.

[16] D. W. Schwendeman, C. W. Wahle, A. K. Kapila, The Riemann problem and a high-resolution Godunov method for a model of compressible two-phase flow, J. Comput. Phys. 212 (2006) 490–526.

[17] D. W. Schwendeman, C. W. Wahle, A. K. Kapila, A study of detonation evolution and structure for a model of compressible two-phase reactive flow, Combust. Theory and Modeling 12 (2008) 159–204.

[18] D. W. Schwendeman, A. K. Kapila, W. D. Henshaw, A study of detonation diffraction and failure for a model of compressible two-phase reactive flow, Combust. Theory and Modeling 14 (2010) 331–266.

[19] R. Abgrall, How to prevent pressure oscillations in mulicomponent flow calculations: A quasi conservative approach, J. Comput. Phys. 125 (1996) 150–160.

[20] R. Saurel, R. Abgrall, A simple method for compressible multifluid flows, SIAM J. Sci. Comput. 21 (3) (1999) 1115–1145.

[21] M. Ozlem, D. W. Schwendeman, A. K. Kapila, W. D. Henshaw, A numerical study of shock-induced cavity collapse, Shock Waves 22 (2012) 89–117.

[22] J. B. Bdzil, R. Menikoff, S. F. Son, A. K. Kapila, D. S. Stewart, Two-phase modeling of deflagration-to-detonation transition in granular materials: A critical examination of modeling issues, Phys. Fluids 11 (2) (1999) 378–402.

[23] W. D. Henshaw, D. W. Schwendeman, An adaptive numerical scheme for high-speed reactive flow on overlapping grids, J. Comput. Phys. 191 (2) (2003) 420–447.

[24] W. D. Henshaw, D. W. Schwendeman, Parallel computation of three-dimensional flows using overlapping grids with adaptive mesh refinement, J. Comput. Phys. 227 (2008) 7469–7502.